Monthly Notices of the ROYAL ASTRONOMICAL SOCIETY

MNRAS **519,** 50–58 (2023) https://doi.org/10.1093/mnras/stac3189
Advance Access publication 2022 November 9

Mapping the circumnuclear regions of the Circinus galaxy with the Imaging X-ray Polarimetry Explorer

F. Ursini [1★] A. Marinucci [2] G. Matt,[1] S. Bianchi [1] F. Marin [3] H. L. Marshall,[4] R. Middei [2] J. Poutanen [5,6] D. Rogantini,[4] A. De Rosa [7] L. Di Gesu,[2] J. A. García,[8] A. Ingram,[9,10] D. E. Kim [7,11,12] H. Krawczynski,[13] S. Puccetti,[2] P. Soffitta,[7] J. Svoboda,[14] F. Tombesi,[12,15,16] M. C. Weisskopf,[17] T. Barnouin,[3] M. Perri,[18,19] J. Podgorny,[3,14,20] A. Ratheesh,[7] A. Zaino,[1] I. Agudo,[21] L. A. Antonelli [18,19] M. Bachetti [22] L. Baldini,[23,24] W. H. Baumgartner,[17] R. Bellazzini,[23] S. D. Bongiorno,[17] R. Bonino [25,26] A. Brez,[23] N. Bucciantini,[27,28,29] F. Capitanio,[7] S. Castellano,[23] E. Cavazzuti,[2] S. Ciprini,[15,19] E. Costa,[7] E. Del Monte,[7] N. Di Lalla,[30] A. Di Marco [7] I. Donnarumma,[2] V. Doroshenko [31] M. Dovciak,[14] S. R. Ehlert [17] T. Enoto,[32] Y. Evangelista,[7] S. Fabiani,[7] R. Ferrazzoli,[7] S. Gunji [33] J. Heyl,[34] W. Iwakiri [35] S. G. Jorstad [36,37] V. Karas,[14] T. Kitaguchi,[32] J. J. Kolodziejczak,[17] F. La Monaca [7] L. Latronico,[25] I. Liodakis [38] S. Maldera,[25] A. Manfreda,[23] A. P. Marscher,[36] I. Mitsuishi,[39] T. Mizuno,[40] F. Muleri,[7] C. Y. Ng,[41] S. L. O'Dell,[17] N. Omodei,[30] C. Oppedisano,[25] A. Papitto,[18] G. G. Pavlov,[42] A. L. Peirson,[30] M. Pesce-Rollins,[23] P.-O. Petrucci,[43] M. Pilia,[22] A. Possenti,[22] B. D. Ramsey,[17] J. Rankin,[7] R. W. Romani,[30] C. Sgrò,[23] P. Slane,[44] G. Spandre,[23] T. Tamagawa,[32] F. Tavecchio,[45] R. Taverna,[46] Y. Tawara,[39] A. F. Tennant,[17] N. E. Thomas,[17] A. Trois [22] S. S. Tsygankov,[5,6] R. Turolla,[46,47] J. Vink [48] K. Wu [47] F. Xie[7,49] and S. Zane[47]

Affiliations are listed at the end of the paper

Accepted 2022 November 1. in original form 2022 October 15

ABSTRACT

We report on the Imaging X-ray Polarimetry Explorer (*IXPE*) observation of the closest and X-ray brightest Compton-thick active galactic nucleus (AGN), the Circinus galaxy. We find the source to be significantly polarized in the 2–6 keV band. From previous studies, the X-ray spectrum is known to be dominated by reflection components, both neutral (torus) and ionized (ionization cones). Our analysis indicates that the polarization degree is 28 ± 7 per cent (at 68 per cent confidence level) for the neutral reflector, with a polarization angle of $18^\circ \pm 5^\circ$, roughly perpendicular to the radio jet. The polarization of the ionized reflection is unconstrained. A comparison with Monte Carlo simulations of the polarization expected from the torus shows that the neutral reflector is consistent with being an equatorial torus with a half-opening angle of 45°–55°. This is the first X-ray polarization detection in a Seyfert galaxy, demonstrating the power of X-ray polarimetry in probing the geometry of the circumnuclear regions of AGNs, and confirming the basic predictions of standard Unification Models.

Key words: polarization – scattering – galaxies: active – galaxies: individual: Circinus – galaxies: Seyfert – X-rays: galaxies.

1 INTRODUCTION

A large fraction of active galactic nuclei (AGNs) are obscured by gas and dust (∼70 per cent of local AGNs; e.g. Ramos Almeida & Ricci 2017). According to Unification Models (e.g. Antonucci 1993), the obscuring medium is a geometrically thick and axisymmetric structure, and is generally referred to as the 'torus'. Sources obscured by material with a column density $N_{\rm H} > \sigma_{\rm T}^{-1} = 1.5 \times 10^{24}$ cm^{-2} (where $\sigma_{\rm T}$ is the Thomson cross-section) are called Compton-thick, and make up a sizeable fraction of local AGNs (∼20–30 per cent; e.g. Malizia et al. 2009; Ricci et al. 2015; Torres-Albà et al. 2021). In general, the X-ray nuclear radiation from Compton-thick Seyfert 2 galaxies is completely obscured, at least up to 10 keV (e.g. Arévalo et al. 2014; Marinucci et al. 2016). The X-ray spectrum is thus dominated by reflection, from both neutral and ionized matter surrounding the nucleus (e.g. Matt et al. 2000). For unobscured objects, the direct emission dominates and the reflection component is weak or even invisible. Compton-thick AGN are therefore ideal candidates for X-ray polarimetric observations aimed at determining the geometry of the circumnuclear scattering material. In fact, the X-ray polarization produced by the reprocessing of the nuclear emission carries information about the cold reflector (i.e. the torus), responsible for the intense iron Kα emission line and Compton reflection continuum, and the ionized reflector, responsible for the soft X-ray continuum and line emission. In particular, it has been

★ E-mail: francesco.ursini@uniroma3.it

shown that measurements of the half-opening angle of the torus and of the inclination angle with respect to the line of sight are possible, along with a comparison of the main axes of the X-ray reflecting structures with those of optical/IR emitting regions, like the ionization cone (e.g. Goosmann & Matt 2011).

The Circinus galaxy is one of the closest AGN (redshift $z = 0.001\,449$; distance $D = 4.2 \pm 0.8$ Mpc; Freeman et al. 1977). It has been extensively observed by X-ray satellites in the last 30 yr. It was detected by *ROSAT* during the All-Sky Survey for the first time in the X-rays (Brinkmann, Siebert & Boller 1994) and later on by the *Advanced Satellite for Cosmology and Astrophysics* (*ASCA*), showing a spectrum dominated by a Compton reflection component (Matt et al. 1996), with a prominent iron Kα emission line and several other lines from lighter elements (Bianchi, Matt & Iwasawa 2001). *Beppo-SAX* confirmed the *ASCA* results below 10 keV and the Compton-thick nature of the source at higher energies (Guainazzi et al. 1999; Matt et al. 1999). The properties of the nuclear and circumnuclear emission have then been investigated in more details thanks to the better angular and spectral resolution of *Chandra* (Sambruna et al. 2001a,b; Marinucci et al. 2013; Kawamuro, Izumi & Imanishi 2019) and *XMM-Newton* (Molendi, Bianchi & Matt 2003; Massaro et al. 2006). *NuSTAR*, more recently, confirmed the Compton-thick nature of the source ($N_{\rm H} > 6 \times 10^{24}$ cm^{-2}; Arévalo et al. 2014). The extranuclear activity of Circinus has also been well-studied at longer wavelengths, showing a prominent [O III] ionization cone (Marconi et al. 1994), two starburst rings at $\sim$2 and 10 arcsec from the nucleus (Wilson et al. 2000, and references therein), and a radio jet has been observed as part of an overall complex extended radio structure (Elmouttie et al. 1998b; Curran, Koribalski & Bains 2008). The 100-pc bipolar jet emanates from the compact core in the same direction of kpc-scale radio plumes (Elmouttie et al. 1998b). On the subparsec scales, the source shows an edge-on, warped accretion disc, traced by H_2O maser emission at 1.3 cm with very long baseline interferometry (Greenhill et al. 2003).

The Circinus galaxy is the X-ray brightest ($F_{2\text{–}10\ \rm keV} \approx 1.5 \times 10^{-11}$ erg cm^{-2} s^{-1}; Bianchi et al. 2002) Compton-thick Seyfert 2 galaxy in the sky. Therefore, it has been chosen as the first Compton-thick AGN to be observed by the *Imaging X-ray Polarimetry Explorer* (*IXPE*; Soffitta et al. 2021; Weisskopf et al. 2022). Here, we report on this observation, performed jointly with *Chandra* to enable a spatially resolved spectro-polarimetric study.

The paper is organized as follows. In Section 2, we describe the *IXPE* and *Chandra* observations and data reduction. In Section 3, we report on the data analysis and results. In Section 4, we discuss the constraints on the geometry of the system by comparing the results with detailed Monte Carlo simulations of the polarization expected from the torus.

2 OBSERVATIONS AND DATA REDUCTION

2.1 *IXPE*

IXPE observed the Circinus galaxy starting on 2022 July 12 with its three detector units (DU)/mirror module assemblies (MMAs), for a net exposure time of 771.5 ks (Table 1). Cleaned level 2 event files were produced and calibrated using standard filtering criteria with the dedicated FTOOLS tasks[1] and the latest calibration files available in the *IXPE* calibration data base (CALDB 20220314).

[1]https://heasarc.gsfc.nasa.gov/docs/ixpe/analysis/IXPE-SOC-DOC-009-UserGuide-Software.pdf

Table 1. Logs of the *IXPE* and *Chandra* observations.

Satellite	Obs. Id.	Start time (UTC)	Net exp. (ks)
IXPE	01003501	2022-07-12	771.5
Chandra	25365	2022-07-11	9.3
	25366	2022-07-24	9.3

The Stokes I, Q, and U background spectra were extracted from source-free circular regions with a radius of 100 arcsec. Extraction radii for the I Stokes spectra of the source were computed via an iterative process that leads to the maximization of the signal-to-noise ratio (SNR) in the 2–8 keV energy band, similar to the approach described in Piconcelli et al. (2004). This procedure consists in the extraction of several source spectra, monotonically increasing the value of the radius, until the maximum SNR is found. We eventually adopted circular regions centred on the source with radii of 52, 52, and 47 arcsec for DU1, DU2, and DU3, respectively. The same extraction radii were then applied to the Q and U Stokes spectra. The weighted analysis method presented in Di Marco et al. (2022; parameter `stokes = Neff` in XSELECT) was applied. We used a constant energy binning of 0.2 keV for Q and U Stokes spectra and required a 2–8 keV SNR higher than 3 in each spectral channel, in the flux spectra. I, Q, and U Stokes spectra from the three DU/MMAs are always fitted independently in the following. Background represents 17.0, 19.7, and 16.4 per cent of the total DU1/MMA1, DU2/MMA2, and DU3/MMA3 I flux spectra, respectively. The same extraction regions were used in IXPEOBSSIM (version 28.2.0: Baldini et al. 2022), which implements the method of Kislat et al. (2015) to reconstruct the polarization properties. The information is represented as data cubes containing images of the Stokes parameters, binned in sky coordinates. Polarization cubes from the source and from the background were extracted, following the same procedure as for MCG-05-23-16 (Marinucci et al. 2022), including background subtraction. We created one polarization cube for each DU in the 2–8 keV band and then combined them; we then computed the Stokes parameters, the corresponding polarization degree and angle, and the associated uncertainties.

2.2 *Chandra*

The central region of the Circinus galaxy is heavily populated by ultraluminous X-ray (ULX) sources (Bauer et al. 2001; Smith & Wilson 2001), and the *IXPE* point spread function ($\simeq$30 arcsec) does not allow us to spatially resolve some of them. For this reason, *Chandra* observed the Circinus galaxy at the beginning and end of the *IXPE* observation. These two *Chandra* observations allowed us to monitor the flux state of the ULXs and in particular of CG X-1, which is highly variable, reaching in the past fluxes almost as large as that of the AGN (Bianchi et al. 2002).

The two *Chandra* observations were performed on 2022 July 11 and 24 (see Table 1) with the Advanced CCD Imaging Spectrometer (ACIS; Garmire et al. 2003) for elapsed times of 10 ks each. To reduce pile-up effects, the frame time was set to 0.5 s and custom CCD subarrays were used. Data were reduced with the Chandra Interactive Analysis of Observations (CIAO; Fruscione et al. 2006) 4.14 and the Chandra Calibration Data Base 4.9.8, adopting standard procedures. At the distance of the source 1 arcsec corresponds to 19 pc. We generated event files for the two observations with the CIAO tool `chandra_repro` and, after cleaning for background flaring, we got net exposure times of 9.3 ks each.

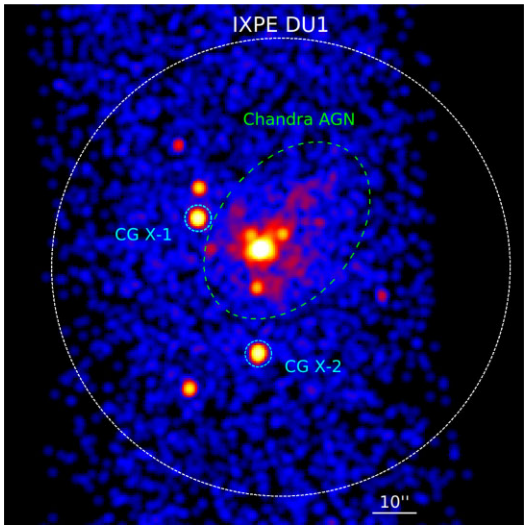

Figure 1. *Chandra* image of the Circinus galaxy (2×2 arcmin^2). The green dashed ellipse marks the *Chandra* extraction region for the AGN (see Section 2.2 for the details). The cyan dotted lines encircle the ULXs CG X-1 and CG X-2. The white dotted circle corresponds to the *IXPE* DU1 extraction region.

The spectra from the CG X-1 and CG X-2 were extracted from circular regions centred on the two sources with 3 arcsec radii. We used a 10 arcsec radius circle for background extraction. For the AGN, we used an ellipse with a semiminor axis of 15 arcsec and semimajor axis of 23 arcsec (Fig. 1). Co-adding the two exposures, in the 2–8 keV band 800 counts are measured for the two ULXs and 4910 counts for the AGN.

After the two ULXs, the brightest point sources in the field, both outside of the AGN extraction region, are CXOU J141312.6–652052 and CXOU J141312.2–652007 (Bauer et al. 2001). However, only 210 counts (2–8 keV) are measured in total for the two sources together. Within the AGN extraction region, three other point sources are detected, namely CXOU J141309.2–652017, CXOU J141310.1–652029, and CXOU J141310.3–652017 (Bauer et al. 2001). Evaluating their counts is less obvious due to the contamination of the AGN; however, we estimate a total of 250 counts (2–8 keV) summing all the three sources. Given the overall small contribution of these sources, for simplicity we only take into account the contribution from CG X-1 and CG X-2 in the following spectral analysis.

Spectra were binned in order to oversample the instrumental resolution by a factor of 3 and to have no less than 30 counts in each background-subtracted spectral channel. This allows the applicability of the χ^2 statistic. We ignored channels between 8 and 10 keV due to pileup, which is not unexpected owing to the decreased effective area of the detector and the decline of the intrinsic source spectrum.[2] We estimate the fraction of detected events that are in fact piled using the CIAO tool `pileup_map`. We infer that in the central 3×3 pixels region the average pile-up fraction is 6 per cent, ranging from 3 to 9 per cent (in the central pixel) for both observations. Details on the analysis of *Chandra* images and spectra are reported in Appendix A. Since the AGN emission is consistent with being constant (see Appendix A), we use the co-added spectrum for the spectro-polarimetric analysis.

[2]For more details, see the Chandra ABC Guide to Pileup, online at: https://cxc.harvard.edu/ciao/download/doc/pileup_abc.pdf.

Table 2. XSPEC measured polarization degrees and angles with associated uncertainties at 68 per cent (1σ) confidence level for one parameter of interest. For the 6–8 keV band, we report the upper limit at 99 per cent confidence level. We note that the polarization angle is undefined when the polarization degree is not significantly detected.

Energy	P.D. (per cent)	P.A. (deg)
2–8 keV	17.6 ± 3.2	16.9 ± 5.3
2–4 keV	16.0 ± 4.9	19.1 ± 8.9
4–6 keV	26.3 ± 5.7	20.2 ± 7.5
2–6 keV	20.0 ± 3.8	19.1 ± 5.5
6–8 keV	<24.5	–

3 POLARIZATION PROPERTIES OF THE CIRCUMNUCLEAR MATTER

In the *IXPE* energy range, the spectrum of the Circinus galaxy is known to be dominated by two components: emission from a warm reflector, likely due to ionized, optically thin matter and mostly contributing below 3 keV, and from a cold reflector dominating the spectrum above 4 keV, due to the optically thick torus (e.g. Bianchi et al. 2001; Sambruna et al. 2001a, b; Massaro et al. 2006). The spectra of both reflectors are composed of a continuum (expected to be significantly polarized) and emission lines (expected to be unpolarized, apart from the contribution by resonant scattering). In Table 2, we report the polarization degree and angle at different energies. We show these parameters as measured from the *IXPE* spectra using XSPEC 12.12.1 (Arnaud 1996), with the 68 per cent confidence level uncertainty for one parameter of interest. The parameters found from the polarization cubes extracted with IXPEOBSSIM are well consistent within the errors. We obtain a significant detection in the 2–6 keV band, with a polarization degree of 20.0 per cent $\pm$ 3.8 per cent (at 68 per cent confidence level). The lack of a significant detection in the 6–8 keV band is likely due to the prominent iron lines present in the spectrum. Indeed, the flux of the iron lines between 6.4 and 7.057 keV reaches 50 per cent of the total flux in the 6–8 keV band (Massaro et al. 2006). The ranges of polarization degree and angle shown in Table 2 are 1D, in the sense that they are derived for each parameter independently of the other. In Fig. 2, we show 2D contour plots of the polarization degree and angle at different energies. We note that in the 2–4 and 4–6 keV bands, the detection significance is greater than 99 per cent, and greater than 3σ at least in the 4–6 keV band. Finally, the polarization angle is consistent with being constant in energy.

We then fit simultaneously the *Chandra* and *IXPE I*, *Q*, and *U* Stokes spectra with a model composed of a power law (for the warm reflector continuum), a PEXRAV (Magdziarz & Zdziarski 1995) component (for the scattered cold reflection continuum) and a number of Gaussian lines.[3] We fix the photon index of PEXRAV at 1.6, consistent with *BeppoSAX*, *Suzaku*, and *NuSTAR* previous measurements (Matt et al. 1999; Yang et al. 2009; Arévalo et al. 2014). We also fix the energy and flux of the Gaussian lines to those derived from the *Chandra*/*HETG* spectrum (not reported here for the sake of brevity; see table 2 of Massaro et al. 2006). No strong variability is expected for these lines, since they are associated with extended emission at kpc scales from the central nuclear source. The warm reflector is partly ionized and it produces a complex emission

[3]The choice of using the PEXRAV model plus emission lines instead of more sophisticated models that treat continuum and lines together is just due to the fact that the polarization of the continuum reflected emission and of the emission lines are expected to be different.

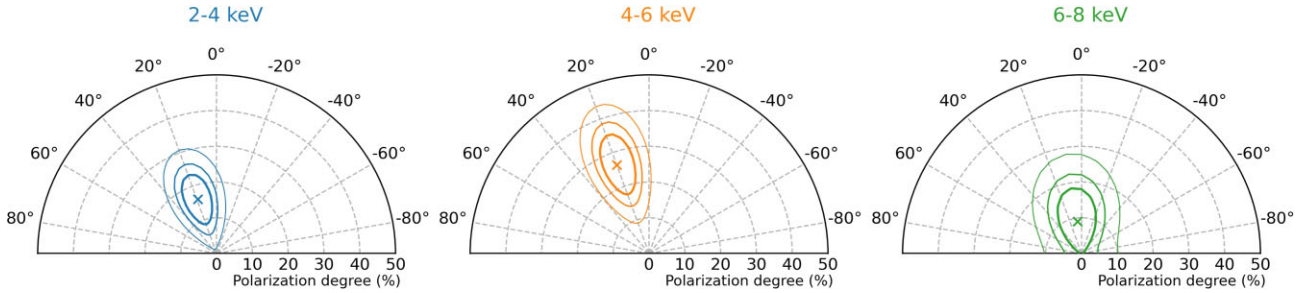

Figure 2. Contour plots of the polarization degree and angle, measured with XSPEC, at the 68 per cent, 90 per cent, and 99 per cent confidence levels, in the 2–4 (left-hand panel, light blue), 4–6 (middle panel, orange), and 6–8 keV (right-hand panel, green) energy bands.

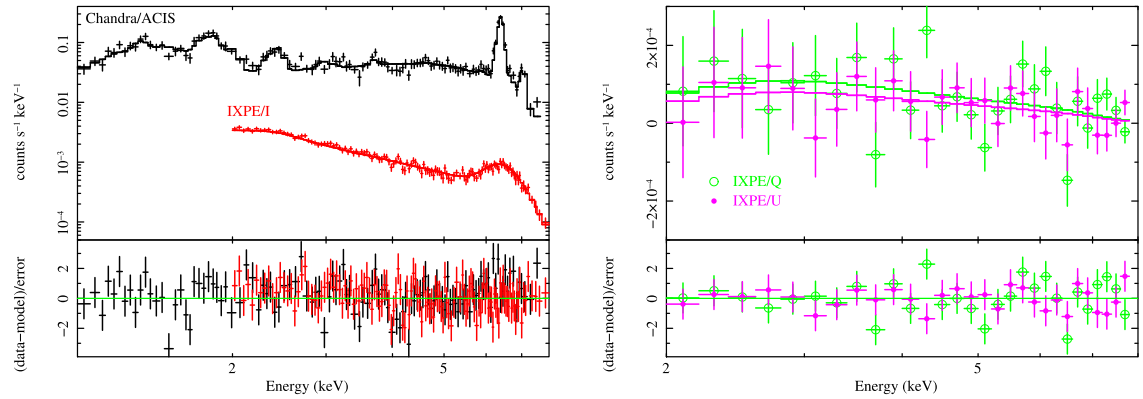

Figure 3. *Left-hand panel: Chandra*/ACIS and *IXPE I* (flux) spectra of the Circinus galaxy with the best-fitting model and the residuals. *Right-hand panel: IXPE Q* and *U* Stokes spectra with the best-fitting model and the residuals. Note the different scale from the left-hand panel. In both panels, *IXPE* spectra are grouped for plotting purposes only (with SETPLOT GROUP in XSPEC).

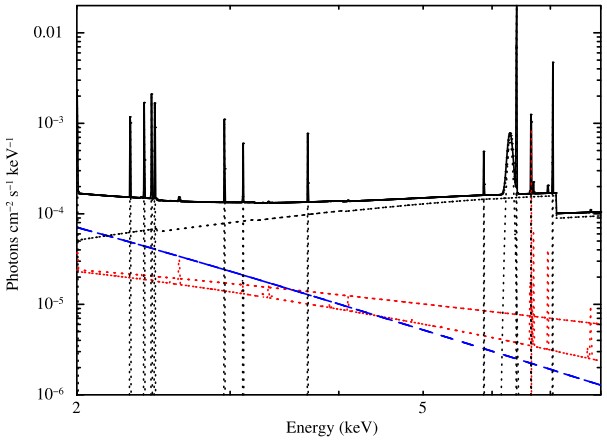

Figure 4. Best-fitting total model (black solid line) in the 2–8 keV band, together with the contribution of various components: cold reflection (black dotted line), warm reflection (blue dashed line), and ULXs (red dotted lines).

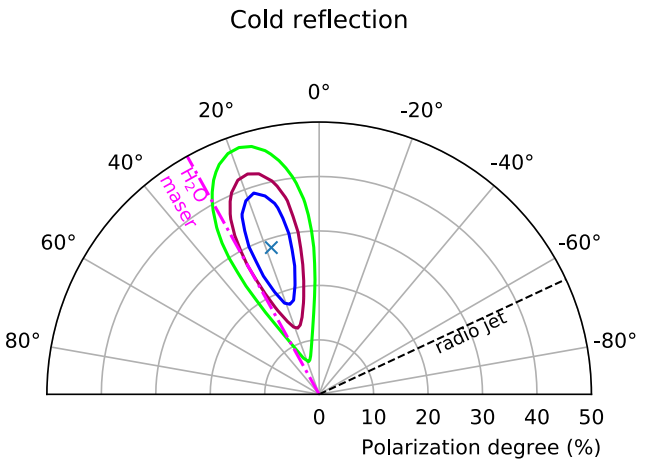

Figure 5. Contour plot of the polarization degree and angle for the cold reflector. The blue, red, and green lines correspond to the 68 per cent, 90 per cent, and 99 per cent confidence levels, respectively. The black dashed line marks the direction of the radio jet, while the magenta dash-dotted line marks the direction of the inner H_2O maser disc.

(e.g. Guainazzi et al. 1999; Kallman et al. 2014). However, it is phenomenologically well described by a soft power law (Bianchi et al. 2001; Marinucci et al. 2013; Arévalo et al. 2014), as often found in obscured Seyfert 2 galaxies (e.g. Bianchi et al. 2001; Matt et al. 2003, 2013; Bauer et al. 2015). We fix its photon index at 3.0 (see Appendix A). For the *IXPE* spectra, we also include the best-fitting model for the ULXs CG X-1 and CG X-2 derived from *Chandra*, keeping all spectral parameters fixed (see Appendix A). The continuum components are multiplied by the POLCONST model, which provides the (energy-independent) polarization degree and angle of each component. We assume the emission lines and the

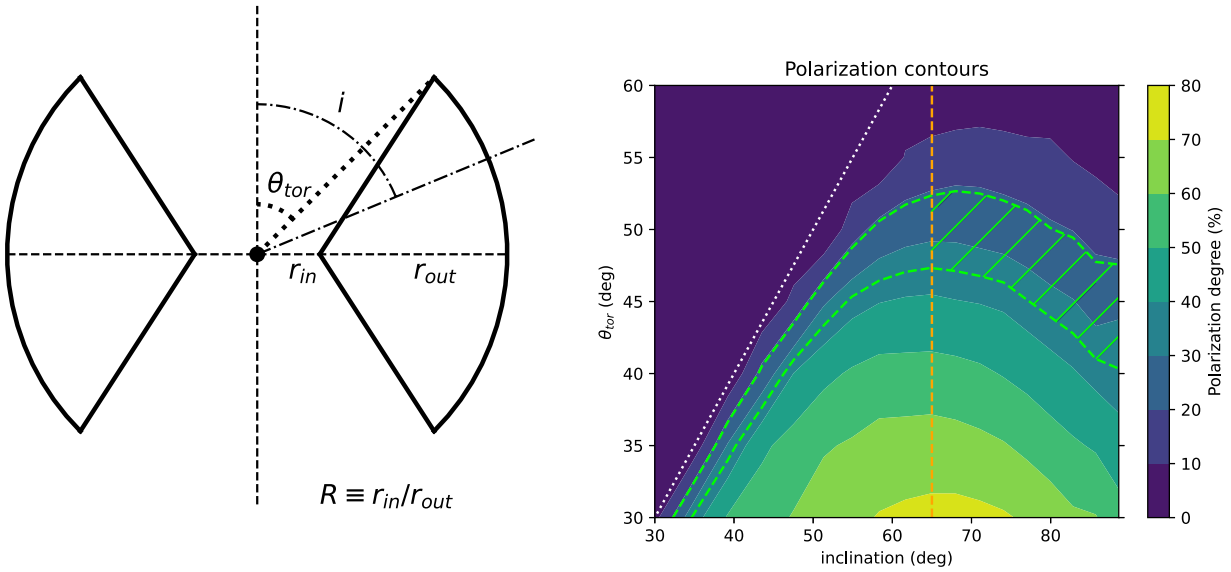

Figure 6. *Left-hand panel:* Sketch of the torus geometry assumed for polarimetric modelling. The torus opening angle $\theta_{\rm tor}$ and the observer inclination i are both measured from the symmetry axis. *Right-hand panel:* Contour plots of the constant polarization degree calculated for scattering off a torus, on the $\theta_{\rm tor} - i$ plane. The white dotted line corresponds to the equality $\theta_{\rm tor} = i$; the condition for the obscuration of the central source is $\theta_{\rm tor} < i$. The green dashed curves enclose the 68 per cent confidence level region on the measured polarization for the cold reflector in the Circinus galaxy. The orange dashed line marks the inclination of the host galaxy, likely a lower limit to the torus inclination (as discussed in the text). The green hatches mark the region of the parameter space consistent with all the observational constraints.

ULXs to be unpolarized.[4] In XSPEC, the model is:

$$\begin{aligned}
&\text{C_CAL} \times \text{TBABS} \times [\text{POLCONST}^{(0)} \times \Big(\sum \text{ZGAUSS}^{(i)} && \text{lines}\\
&\quad + \text{POWERLAW} && \text{CG X-1}\\
&\quad + \text{RAYMOND} + \text{ZGAUSS}\Big) && \text{CG X-2}\\
&\quad + \text{POLCONST}^{(w)} \times \text{POWERLAW} && \text{warm refl.}\\
&\quad + \text{POLCONST}^{(c)} \times \text{PEXRAV}] && \text{cold refl.}
\end{aligned}$$

where C_CAL denotes the cross-calibration constant. We keep the polarization degree of POLCONST$^{(0)}$ fixed at zero, which is needed to assume an unpolarized component in XSPEC. Assuming that the warm and cold reflectors are both axially symmetric structures, their polarization angle is expected to be either parallel or perpendicular to the common symmetry axis. For simplicity, we assume the same polarization angle for the warm and cold reflectors. However, we obtain consistent results assuming orthogonal vectors, or by leaving the two polarization angles untied. The fit is very good, with χ^2/d.o.f. = 702/662. The data and best-fitting model are shown in Figs 3 and 4. The best-fitting parameters, and in particular the polarization degree and angle, are reported in Table 3 and Fig. 5. The polarization degree of the warm reflector is unconstrained, due to its relatively low flux (20 ± 5 per cent of the total flux

[4]If we fit for the polarization of the Fe Kα line complex, we obtain an upper limit of 20 per cent, consistent with the expectation for unpolarized fluorescence emission. On the other hand, the Compton shoulder, due to the downscattering of line photons, could theoretically be polarized up to 15 per cent (as computed with the code of Ghisellini, Haardt & Matt 1994). However, its flux is at most 20 per cent of that of the line core (Bianchi et al. 2002; Molendi et al. 2003). Therefore, the overall polarization of the line complex should be in any case less than 3 per cent, and we choose to neglect it in the spectral fit.

Table 3. Best-fitting parameters (68 per cent confidence level for one parameter of interest) of the joint *Chandra* and *IXPE* fit. Normalizations are in units of photons keV^{-1} cm^{-2} s^{-1}, while the flux is in unit of erg cm^{-2} s^{-1}. (f) denotes a fixed parameter.

Parameter	Value
CG X-1 (POWERLAW)	
Γ	1.1(f)
N	6×10^{-5}(f)
CG X-2 (RAYMOND + ZGAUSS)	
$kT_{\rm RAYMOND}$ (keV)	10(f)
$N_{\rm RAYMOND}$	3×10^{-4}(f)
$E_{\rm ZGAUSS}$ (keV)	6.67(f)
$N_{\rm ZGAUSS}$ (keV)	7.9×10^{-6}(f)
Cold reflector (PEXRAV)	
Γ	1.6(f)
N	$(2.06 \pm 0.04) \times 10^{-2}$
P.D. (%)	28 ± 7
P.A. (deg)	18 ± 5
Warm reflector (POWERLAW)	
Γ	3.0(f)
N	6.6×10^{-4}(f)
P.D. (%)	unconstrained
P.A. (deg)	=18
Cross-calibration constants	
$C_{\rm DU1\text{-}ACIS}$	0.809 ± 0.014
$C_{\rm DU2\text{-}ACIS}$	0.723 ± 0.013
$C_{\rm DU3\text{-}ACIS}$	0.677 ± 0.012
Observed flux	
$F_{\rm 2\text{-}8keV}$	$(1.00 \pm 0.01) \times 10^{-11}$
χ^2/d.o.f.	702/662

in the 2–4 keV band; see also Fig. 4). For the cold reflector, instead, we obtain significant constraints: a polarization degree of 28 ± 7 per cent and a polarization angle of $18^\circ \pm 5^\circ$ (68 per cent confidence for one parameter; see also the two-parameter contours in Fig. 5). Interestingly, the polarization angle is consistent with being perpendicular to the radio jet (position angle of 295°; Elmouttie et al. 1998b), which also roughly coincides with the axis of the Hα ionization cone (Elmouttie et al. 1998a), and is close to the direction of the inner H_2O maser disc (position angle of $29^\circ \pm 3^\circ$; Greenhill et al. 2003).

We also note that the ULXs could in principle be polarized, however, they are subdominant at all energies (see Fig. 4). Even if we assume a polarization degree of 10 per cent for the ULXs, the fit discussed above is essentially unchanged. Thus, unless highly polarized (which is unlikely, see e.g. Krawczynski et al. 2022; Vink et al. 2022), the ULXs cannot affect the AGN measurement.

4 DISCUSSION AND CONCLUSIONS

The radiation reflected off the torus, assumed to have an axial symmetry, is expected to be highly polarized (Ghisellini et al. 1994; Goosmann & Matt 2011; Marin et al. 2018; Ratheesh et al. 2021), with a polarization degree depending on the geometrical parameters (namely the torus aperture and the system's inclination) and a polarization angle orthogonal to the torus axis. To better explore the polarization properties of the reflecting torus, we perform calculations with the Monte Carlo radiative transfer code described in Ghisellini et al. (1994). The code takes into account Compton scattering and photoelectric absorption in a neutral medium with solar abundances (see also Matt, Perola & Piro 1991). Ratheesh et al. (2021) applied the code to compute the polarization degree of radiation scattered by a torus-like distribution. We show in Fig. 6 (left-hand panel) a sketch of the assumed geometry. The shape of the torus is defined by the half-opening angle $\theta_{\rm tor}$ and the ratio R between the inner and outer radius. Like Ratheesh et al. (2021), we assume two different values $R = 0.1$ and 0.5. As for the equatorial column density, we assume $N_{\rm H} = 1 \times 10^{25}$ cm^{-2}, consistent with the X-ray measurements of Arévalo et al. (2014).

In Fig. 6 (right-hand panel), we show the contours of the polarization degree, calculated as a function of the inclination and of the torus aperture. The 68 per cent confidence level region for the observed value of polarization is also shown. We only plot the case with $R = 0.1$, because $R = 0.5$ yields very similar results. Assuming an observer inclination of 65°, namely that of the host galaxy (Freeman et al. 1977), we would obtain a torus aperture roughly in the range 45°–55°. However, the actual inclination might be larger, and different measurements are consistent with an edge-on torus. From the CO(3-2) emission within the central 10 pc, Izumi et al. (2018) estimate $i > 70^\circ$ and note that the inclination could increase at lower radii. Indeed, for the 1-pc scale mid-infrared disc, Tristram et al. (2014) estimate $i > 75^\circ$, while Isbell et al. (2022) report $i > 83^\circ$. As suggested by Izumi et al. (2018) and Isbell et al. (2022), the inclination could reach 90° for the H_2O maser disc (Greenhill et al. 2003). Assuming a torus close to edge-on, we obtain an aperture of 40°–50°. Finally, Elmouttie et al. (1998a) estimate a value of 33° for the half-opening angle of the Hα cone, while Fischer et al. (2013) estimate 41° for the [O III] cone. This implies a lower limit to the torus aperture, which is consistent with our calculations.

A torus-like distribution of gas and dust surrounding the central engine is the cornerstone of AGN Unification Models, notwithstanding their continuing development (e.g. Antonucci & Miller 1985; Antonucci 1993; Bianchi, Maiolino & Risaliti 2012; Marin 2014; Netzer 2015; Marin 2016; Ramos Almeida & Ricci 2017). In the current understanding, the torus is actually a clumpy structure, as was early on suggested by Krolik & Begelman (1988). Especially in the case of the Circinus galaxy, this is strongly supported by infrared interferometry (Tristram et al. 2007, 2014; Stalevski, Asmus & Tristram 2017; Stalevski, Tristram & Asmus 2019; Isbell et al. 2022) and by the imaging analysis of the X-ray reflector (Marinucci et al. 2013; see also Andonie et al. 2022). In any case, the X-ray polarimetric properties are in qualitative agreement with the expected results for a geometrically thick torus having an aspect ratio $h/r \sim 1$, meaning a covering factor $\cos\theta_{\rm tor} \sim 0.7$. This result is consistent with the estimate obtained for local AGNs from the average X-ray absorption properties (see Ramos Almeida & Ricci 2017, and references therein).

We note that the Unification Model was introduced after the detection of broad emission lines in the optical polarized spectrum of Seyfert 2 galaxies, with the first one being the Compton-thick AGN NGC 1068 (Antonucci & Miller 1985; see also Oliva et al. 1998 for the case of the Circinus galaxy). Adding a crucial piece of information, X-ray polarimetry now confirms the basic picture of this scenario. A comprehensive discussion of its implications, taking into account polarimetric information at all wavelengths (e.g. Marin 2018), is beyond the scope of this paper and will be the subject of a future work.

ACKNOWLEDGEMENTS

The Imaging X ray Polarimetry Explorer (IXPE) is a joint US and Italian mission. The US contribution is supported by the National Aeronautics and Space Administration (NASA) and led and managed by its Marshall Space Flight Center (MSFC), with industry partner Ball Aerospace (contract NNM15AA18C). The Italian contribution is supported by the Italian Space Agency (Agenzia Spaziale Italiana, ASI) through contract ASI-OHBI-2017-12-I.0, agreements ASI-INAF-2017-12-H0 and ASI-INFN-2017.13-H0, and its Space Science Data Center (SSDC) with agreements ASI-INAF-2022-14-HH.0 and ASI-INFN 2021-43-HH.0, and by the Istituto Nazionale di Astrofisica (INAF) and the Istituto Nazionale di Fisica Nucleare (INFN) in Italy. This research used data products provided by the IXPE Team (MSFC, SSDC, INAF, and INFN) and distributed with additional software tools by the High-Energy Astrophysics Science Archive Research Center (HEASARC), at NASA Goddard Space Flight Center (GSFC). JPou and SST were supported by the Academy of Finland grants 349373 and 349906. AIng acknowledges support from the Royal Society. MDov, JSvo, and VKar acknowledge the support from the GACR project 21-06825X. POP acknowledges financial support from the French High Energy Program (PNHE/CNRS) and from the French spatial agency (CNES).

DATA AVAILABILITY

The data used in this paper are publicly available in the HEASARC data base. The code by Ghisellini et al. (1994) used to perform the numerical simulations is proprietary; simulation data supporting the findings of the article will be shared on reasonable request.

REFERENCES

Andonie C., Ricci C., Paltani S., Arévalo P., Treister E., Bauer F., Stalevski M., 2022, MNRAS, 511, 5768

Antonucci R., 1993, ARA&A, 31, 473
Antonucci R. R. J., Miller J. S., 1985, ApJ, 297, 621
Arévalo P. et al., 2014, ApJ, 791, 81
Arnaud K. A., 1996, in Jacoby G. H., Barnes J., eds, ASP Conf. Ser., Vol. 101, Astronomical Data Analysis Software and Systems V. Astron. Soc. Pac., San Francisco, p. 17
Baldini L., Bucciantini N., Di Lalla N., Ehlert S. R., Manfreda A., Omodei N., Pesce-Rollins M., Sgrò C., 2022, SoftwareX, 19, article id. 101194
Bauer F. E., Brandt W. N., Sambruna R. M., Chartas G., Garmire G. P., Kaspi S., Netzer H., 2001, AJ, 122, 182
Bauer F. E. et al., 2015, ApJ, 812, 116
Bianchi S., Matt G., Iwasawa K., 2001, MNRAS, 322, 669
Bianchi S., Matt G., Fiore F., Fabian A. C., Iwasawa K., Nicastro F., 2002, A&A, 396, 793
Bianchi S., Maiolino R., Risaliti G., 2012, Adv. Astron., 2012, 782030
Brinkmann W., Siebert J., Boller T., 1994, A&A, 281, 355
Curran S. J., Koribalski B. S., Bains I., 2008, MNRAS, 389, 63
Di Marco A. et al., 2022, AJ, 163, 170
Elmouttie M., Koribalski B., Gordon S., Taylor K., Houghton S., Lavezzi T., Haynes R., Jones K., 1998a, MNRAS, 297, 49
Elmouttie M., Haynes R. F., Jones K. L., Sadler E. M., Ehle M., 1998b, MNRAS, 297, 1202
Esposito P., Israel G. L., Milisavljevic D., Mapelli M., Zampieri L., Sidoli L., Fabbiano G., Rodríguez Castillo G. A., 2015, MNRAS, 452, 1112
Fischer T. C., Crenshaw D. M., Kraemer S. B., Schmitt H. R., 2013, ApJS, 209, 1
Freeman K. C., Karlsson B., Lynga G., Burrell J. F., van Woerden H., Goss W. M., Mebold U., 1977, A&A, 55, 445
Fruscione A. et al., 2006, in Silva D. R. E. D. R., eds, Proc. SPIE Conf. Ser., Vol. 6270, Observatory Operations: Strategies, Processes, and Systems. SPIE, Bellingham, p. 62701V
Garmire G. P., Bautz M. W., Ford P. G., Nousek J. A., Ricker G. R., 2003, in Truemper J. E. D. T. H., eds, Proc. SPIE Conf. Ser., Vol. 4851, X-Ray and Gamma-Ray Telescopes and Instruments for Astronomy. SPIE, Bellingham, p. 28
Ghisellini G., Haardt F., Matt G., 1994, MNRAS, 267, 743
Goosmann R. W., Matt G., 2011, MNRAS, 415, 3119
Greenhill L. J. et al., 2003, ApJ, 590, 162
Guainazzi M. et al., 1999, MNRAS, 310, 10
Isbell J. W. et al., 2022, A&A, 663, A35
Izumi T., Wada K., Fukushige R., Hamamura S., Kohno K., 2018, ApJ, 867, 48
Kallman T., Evans D. A., Marshall H., Canizares C., Longinotti A., Nowak M., Schulz N., 2014, ApJ, 780, 121
Kawamuro T., Izumi T., Imanishi M., 2019, PASJ, 71, 68
Kislat F., Clark B., Beilicke M., Krawczynski H., 2015, Astropart. Phys., 68, 45
Krawczynski H. et al., 2022, Science, 378, 650
Krolik J. H., Begelman M. C., 1988, ApJ, 329, 702
Magdziarz P., Zdziarski A. A., 1995, MNRAS, 273, 837
Malizia A., Stephen J. B., Bassani L., Bird A. J., Panessa F., Ubertini P., 2009, MNRAS, 399, 944
Marconi A., Moorwood A. F. M., Origlia L., Oliva E., 1994, The Messenger, 78, 20
Marin F., 2014, MNRAS, 441, 551
Marin F., 2016, MNRAS, 460, 3679
Marin F., 2018, MNRAS, 479, 3142
Marin F., Dovčiak M., Muleri F., Kislat F. F., Krawczynski H. S., 2018, MNRAS, 473, 1286
Marinucci A., Miniutti G., Bianchi S., Matt G., Risaliti G., 2013, MNRAS, 436, 2500
Marinucci A. et al., 2016, MNRAS, 456, L94
Marinucci A. et al., 2022, MNRAS, 516, 5907
Massaro F., Bianchi S., Matt G., D'Onofrio E., Nicastro F., 2006, A&A, 455, 153
Matt G., Perola G. C., Piro L., 1991, A&A, 247, 25
Matt G. et al., 1996, MNRAS, 281, L69
Matt G. et al., 1999, A&A, 341, L39
Matt G., Fabian A. C., Guainazzi M., Iwasawa K., Bassani L., Malaguti G., 2000, MNRAS, 318, 173
Matt G., Bianchi S., Guainazzi M., Brandt W. N., Fabian A. C., Iwasawa K., Perola G. C., 2003, A&A, 399, 519
Matt G., Bianchi S., Marinucci A., Guainazzi M., Iwawasa K., Jimenez Bailon E., 2013, A&A, 556, A91
Molendi S., Bianchi S., Matt G., 2003, MNRAS, 343, L1
Netzer H., 2015, ARA&A, 53, 365
Oliva E., Marconi A., Cimatti A., di Serego Alighieri S., 1998, A&A, 329, L21
Piconcelli E., Jimenez-Bailón E., Guainazzi M., Schartel N., Rodríguez-Pascual P. M., Santos-Lleó M., 2004, MNRAS, 351, 161
Qiu Y. et al., 2019, ApJ, 877, 57
Ramos Almeida C., Ricci C., 2017, Nature Astron., 1, 679
Ratheesh A., Matt G., Tombesi F., Soffitta P., Pesce-Rollins M., Di Marco A., 2021, A&A, 655, A96
Ricci C., Ueda Y., Koss M. J., Trakhtenbrot B., Bauer F. E., Gandhi P., 2015, ApJ, 815, L13
Sambruna R. M., Brandt W. N., Chartas G., Netzer H., Kaspi S., Garmire G. P., Nousek J. A., Weaver K. A., 2001a, ApJ, 546, L9
Sambruna R. M., Netzer H., Kaspi S., Brandt W. N., Chartas G., Garmire G. P., Nousek J. A., Weaver K. A., 2001b, ApJ, 546, L13
Smith D. A., Wilson A. S., 2001, ApJ, 557, 180
Soffitta P. et al., 2021, AJ, 162, 208
Stalevski M., Asmus D., Tristram K. R. W., 2017, MNRAS, 472, 3854
Stalevski M., Tristram K. R. W., Asmus D., 2019, MNRAS, 484, 3334
Torres-Albà N. et al., 2021, ApJ, 922, 252
Tristram K. R. W. et al., 2007, A&A, 474, 837
Tristram K. R. W., Burtscher L., Jaffe W., Meisenheimer K., Hönig S. F., Kishimoto M., Schartmann M., Weigelt G., 2014, A&A, 563, A82
Vink J. et al., 2022, ApJ, 938
Weisskopf M. C., Wu K., Tennant A. F., Swartz D. A., Ghosh K. K., 2004, ApJ, 605, 360
Weisskopf M. C. et al., 2022, J. Astron. Telesc. Instrum. Syst., 8, 026002
Wilson A. S., Shopbell P. L., Simpson C., Storchi-Bergmann T., Barbosa F. K. B., Ward M. J., 2000, AJ, 120, 1325
Yang Y., Wilson A. S., Matt G., Terashima Y., Greenhill L. J., 2009, ApJ, 691, 131

APPENDIX A: *CHANDRA* OBSERVATIONS AND ANALYSIS

Chandra performed two 10-ks observations at the beginning (2022 July 11, obs1) and end (2022 July 24, obs2) of the *IXPE* observation, to monitor the flux state of the variable ULXs in the Circinus Galaxy, as well as the AGN spectrum. The *Chandra* image of obs1 is shown in Fig. 1. We analysed the spectra of CG X-1 and CG X-2 to account for these sources in the *IXPE* spectral analysis.

The nature of CG X-1 has been debated in the literature (Bauer et al. 2001; Bianchi et al. 2002; Weisskopf et al. 2004; Esposito et al. 2015), however, its spectral and variability properties are consistent with an eclipsing Wolf–Rayet ULX (Esposito et al. 2015; Qiu et al. 2019). In any case, its spectrum is well-described by a variable power law. We find a good fit of the two spectra from obs1 and obs2 (χ^2/d.o.f. = 109/106), with a photon index $\Gamma = 0.9 \pm 0.2$ in obs1 and 1.30 ± 0.17 in obs2. The 1–8 keV flux increases by a factor of $\sim$2 between the two pointings, from $(3.7 \pm 0.5) \times 10^{-13}$ to $(7.2 \pm 0.5) \times 10^{-13}$ erg cm^{-2} s^{-1}. The spectra are shown in Fig. A1 (top panel). When modelling the *IXPE* spectrum, we opt to include a power law with average parameters, namely $\Gamma = 1.1$ and a 1–8 keV flux of 5.45×10^{-13} erg cm^{-2} s^{-1}.

CG X-2 is a supernova remnant candidate (Bauer et al. 2001). Following Bauer et al. (2001), we fit the spectrum with a Raymond–Smith thermal plasma with a temperature of 10 keV, plus a Gaussian

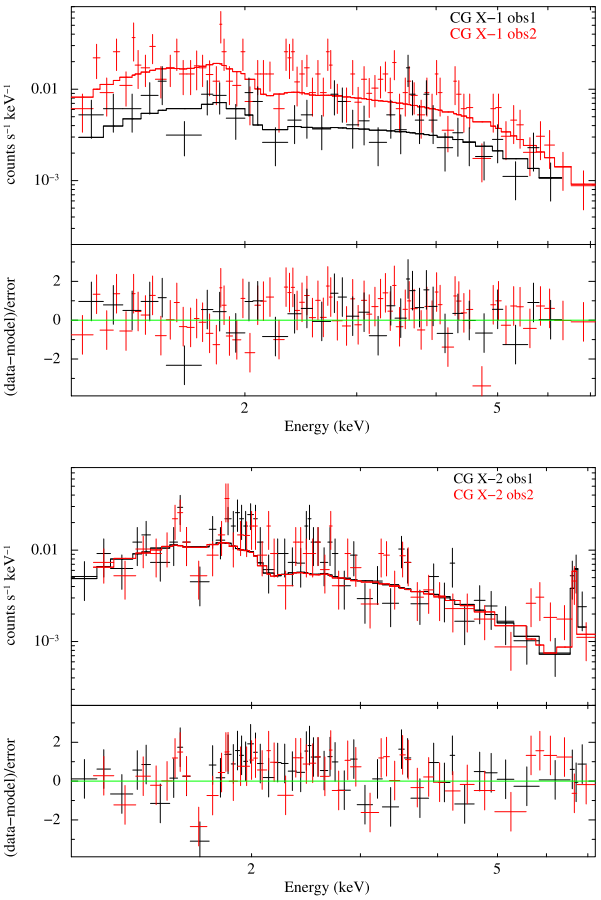

Figure A1. *Chandra*/ACIS spectra of CG X-1 (top) and CG X-2 (bottom) with the best-fitting model in the 1–8 keV band. The black and red coloured crosses correspond to observation 1 and 2, respectively.

line for ionized iron emission (see also Bianchi et al. 2002). We jointly fit the two observations, as we find no significant variability among them. We find a decent fit (χ^2/d.o.f. $= 118/102$) with a narrow Gaussian line at 6.67 ± 0.05 keV having a flux of $(8 \pm 4) \times 10^{-6}$ ph cm^{-2} s^{-1}. The total model flux is $(4.8 \pm 0.3) \times 10^{-13}$ erg cm^{-2} s^{-1}. We show the spectra in Fig. A1 (bottom panel).

Besides *Chandra*, *Swift*/XRT also performed two observations of the Circinus field, centred on CG X-2, on 2022 July 18 and July 20 (ObsIds 00045807010 and 00045807011) for an exposure time of 4.3 and 4.6 ks, respectively. The small number of counts in XRT prevents a detailed analysis; however, we find no evidence for a significant flux variability of CG X-1 and CG X-2 during these observations.

Finally, we fit the spectrum of the AGN, with a model including cold reflection (PEXRAV) and Gaussian emission lines (Massaro et al. 2006). As a first step, we jointly fit obs1 and obs2 keeping all parameters tied. We obtain a poor fit with χ^2/d.o.f. $= 340/135$, with significant residuals below 2 keV. Next, we include a power law to describe warm reflection, and we fix the PEXRAV photon index at 1.6 to avoid model degeneracies. We obtain an acceptable fit with χ^2/d.o.f. $= 179/134$, with no prominent residuals (see Fig. A2). For the warm reflection power law, we obtain a photon index of 3.0 ± 0.2, consistent with the value reported by Marinucci et al. (2013) from *Chandra* data. The flux contribution of this component is 5–10 per cent of the total in the 1–8 keV band, raising to ∼20 per cent in the 2–4 keV band. We do not find a significant improvement by leaving the parameters free to vary between the two observations.

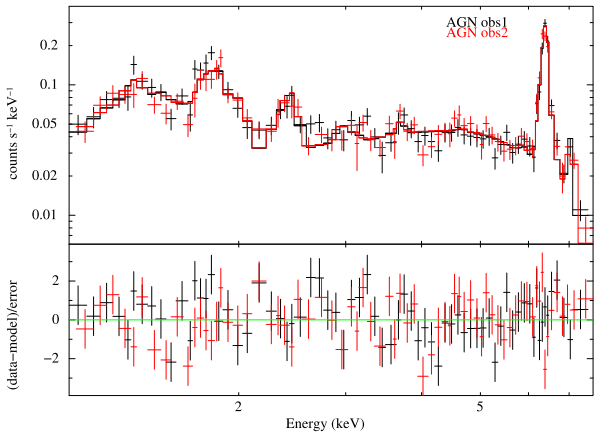

Figure A2. *Chandra*/ACIS spectra of the AGN with the best-fitting model in the 1–8 keV band. The black and red coloured crosses correspond to observation 1 and 2, respectively.

We also do not find a significant improvement by leaving free the PEXRAV photon index. In the *IXPE* energy band (2–8 keV), the flux of the AGN is $(1.04 \pm 0.02) \times 10^{-11}$ erg cm^{-2} s^{-1}, while that of CG X-1 and CG X-2 is respectively 3–6 per cent and 4 per cent of the AGN flux.

[1]*Dipartimento di Matematica e Fisica, Università degli Studi Roma Tre, via della Vasca Navale 84, I-00146 Roma, Italy*
[2]*ASI - Agenzia Spaziale Italiana, Via del Politecnico snc, I-00133 Roma, Italy*
[3]*Université de Strasbourg, CNRS, Observatoire Astronomique de Strasbourg, UMR 7550, F-67000 Strasbourg, France*
[4]*Kavli Institute for Astrophysics and Space Research, Massachusetts Institute of Technology, 77 Massachusetts Ave., Cambridge, MA 02139, USA*
[5]*Department of Physics and Astronomy, FI-20014 University of Turku, Finland*
[6]*Space Research Institute of the Russian Academy of Sciences, Profsoyuznaya Str. 84/32, Moscow 117997, Russia*
[7]*INAF Istituto di Astrofisica e Planetologia Spaziali, Via del Fosso del Cavaliere 100, I-00133 Roma, Italy*
[8]*Cahill Center for Astronomy and Astrophysics, California Institute of Technology, Pasadena, CA 91125, USA*
[9]*Department of Physics - Astrophysics, University of Oxford, Denys Wilkinson Building, Keble Road, Oxford OX1 3RH, UK*
[10]*School of Mathematics, Statistics and Physics, Newcastle University, Herschel Building, Newcastle upon Tyne NE1 7RU, UK*
[11]*Dipartimento di Fisica, Universitá degli Studi di Roma 'La Sapienza', Piazzale Aldo Moro 5, I-00185 Roma, Italy*
[12]*Dipartimento di Fisica, Universitá degli Studi di Roma 'Tor Vergata', Via della Ricerca Scientifica 1, I-00133 Roma, Italy*
[13]*Physics Department and McDonnell Center for the Space Sciences, Washington University in St. Louis, St. Louis, MO 63130, USA*
[14]*Astronomical Institute of the Czech Academy of Sciences, Boční II 1401/1, CZ-14100 Praha 4, Czech Republic*
[15]*Istituto Nazionale di Fisica Nucleare, Sezione di Roma 'Tor Vergata', Via della Ricerca Scientifica 1, I-00133 Roma, Italy*
[16]*Department of Astronomy, University of Maryland, College Park, Maryland 20742, USA*
[17]*NASA Marshall Space Flight Center, Huntsville, AL 35812, USA*
[18]*INAF Osservatorio Astronomico di Roma, Via Frascati 33, I-00078 Monte Porzio Catone (RM), Italy*
[19]*Space Science Data Center, Agenzia Spaziale Italiana, Via del Politecnico snc, I-00133 Roma, Italy*
[20]*Astronomical Institute, Charles University, V Holešovičkách 2, CZ-18000 Prague, Czech Republic*

[21]*Instituto de Astrofísica de Andalucía-CSIC, Glorieta de la Astronomía s/n, E-18008 Granada, Spain*
[22]*INAF Osservatorio Astronomico di Cagliari, Via della Scienza 5, I-09047 Selargius (CA), Italy*
[23]*Istituto Nazionale di Fisica Nucleare, Sezione di Pisa, Largo B. Pontecorvo 3, I-56127 Pisa, Italy*
[24]*Dipartimento di Fisica, Universitá di Pisa, Largo B. Pontecorvo 3, I-56127 Pisa, Italy*
[25]*Istituto Nazionale di Fisica Nucleare, Sezione di Torino, Via Pietro Giuria 1, I-10125 Torino, Italy*
[26]*Dipartimento di Fisica, Universitá degli Studi di Torino, Via Pietro Giuria 1, I-10125 Torino, Italy*
[27]*INAF Osservatorio Astrofisico di Arcetri, Largo Enrico Fermi 5, I-50125 Firenze, Italy*
[28]*Dipartimento di Fisica e Astronomia, Universitá degli Studi di Firenze, Via Sansone 1, I-50019 Sesto Fiorentino (FI), Italy*
[29]*Istituto Nazionale di Fisica Nucleare, Sezione di Firenze, Via Sansone 1, I-50019 Sesto Fiorentino (FI), Italy*
[30]*Department of Physics and Kavli Institute for Particle Astrophysics and Cosmology, Stanford University, Stanford, California 94305, USA*
[31]*Institut für Astronomie und Astrophysik, Universität Tübingen, Sand 1, D-72076 Tübingen, Germany*
[32]*RIKEN Cluster for Pioneering Research, 2-1 Hirosawa, Wako, Saitama 351-0198, Japan*
[33]*Yamagata University, 1-4-12 Kojirakawa-machi, Yamagata-shi 990-8560, Japan*
[34]*University of British Columbia, Vancouver, BC V6T 1Z4, Canada*
[35]*Department of Physics, Faculty of Science and Engineering, Chuo University, 1-13-27 Kasuga, Bunkyo-ku, Tokyo 112-8551, Japan*
[36]*Institute for Astrophysical Research, Boston University, 725 Commonwealth Avenue, Boston, MA 02215, USA*
[37]*Department of Astrophysics, St. Petersburg State University, Universitetsky pr. 28, Petrodvoretz, 198504 St. Petersburg, Russia*
[38]*Finnish Centre for Astronomy with ESO, 20014 University of Turku, Turku 20014, Finland*
[39]*Graduate School of Science, Division of Particle and Astrophysical Science, Nagoya University, Furo-cho, Chikusa-ku, Nagoya, Aichi 464-8602, Japan*
[40]*Hiroshima Astrophysical Science Center, Hiroshima University, 1-3-1 Kagamiyama, Higashi-Hiroshima, Hiroshima 739-8526, Japan*
[41]*Department of Physics, The University of Hong Kong, Pokfulam, Hong Kong*
[42]*Department of Astronomy and Astrophysics, Pennsylvania State University, University Park, PA 16802, USA*
[43]*Université Grenoble Alpes, CNRS, IPAG, F-38000 Grenoble, France*
[44]*Center for Astrophysics | Harvard & Smithsonian, 60 Garden St, Cambridge, MA 02138, USA*
[45]*INAF Osservatorio Astronomico di Brera, Via E. Bianchi 46, I-23807 Merate (LC), Italy*
[46]*Dipartimento di Fisica e Astronomia, Universitá degli Studi di Padova, Via Marzolo 8, I-35131 Padova, Italy*
[47]*Mullard Space Science Laboratory, University College London, Holmbury St Mary, Dorking, Surrey RH5 6NT, UK*
[48]*Anton Pannekoek Institute for Astronomy & GRAPPA, University of Amsterdam, Science Park 904, NL-1098 XH Amsterdam, the Netherlands*
[49]*Guangxi Key Laboratory for Relativistic Astrophysics, School of Physical Science and Technology, Guangxi University, Nanning 530004, China*

This paper has been typeset from a TEX/LATEX file prepared by the author.